Optical anisotropy of the $J_{\text{eff}} = 1/2$ Mott insulator Sr_2IrO_4

D. Pröpper,[1] A. N. Yaresko,[1] M. Höppner,[1] Y. Matiks,[1] Y.-L. Mathis,[2] T. Takayama,[1,3] A. Matsumoto,[1,3] H. Takagi,[1,3]
B. Keimer,[1] and A. V. Boris[1]

[1]*Max-Planck-Institut für Festkörperforschung, Heisenbergstraße 1, 70569 Stuttgart, Germany*
[2]*Synchrotron Facility ANKA, Karlsruhe Institute of Technology, 76344 Eggenstein - Leopoldshafen, Germany*
[3]*Department of Physics, University of Tokyo, Hongo, Tokyo 113-0033, Japan*

We report the complex dielectric function along and perpendicular to the IrO_2 planes in the layered perovskite Sr_2IrO_4 determined by spectroscopic ellipsometry in the spectral range from 12 meV to 6 eV. Thin high-quality single crystals were stacked to measure the c-axis optical conductivity. In the phonon response, we identified ten infrared-active modes polarized within the basal plane and only four modes polarized along the c axis, which we assign according to first-principles lattice dynamics calculations. We also observed a strong optical anisotropy in the near-infrared spectra. It arises from direct transitions between Ir $5d$ t_{2g} $J_{\text{eff}} = 1/2$ and $J_{\text{eff}} = 3/2$ bands, whose transition probability is highly suppressed for light polarized along the c axis. The spectra are analyzed and discussed in terms of relativistic local spin-density approximation (LSDA)$+U$ band structure calculations.

I. INTRODUCTION

A rich variety of electronic ground states of transition-metal oxides (TMOs) emerges from strong electron correlations and cooperative phenomena with competing interactions, including the on-site Coulomb repulsion U, crystal-electric field (CEF), and spin-orbit coupling (SOC). The transition from elements with $3d$ via $4d$ to $5d$ valence orbitals progressively results in larger single-particle bandwidth W, reduced U, and enhanced SOC. TMOs of the type $(La,Sr)_2MO_4$, where M = Cu ($3d$), Ru ($4d$), or Ir ($5d$), allow one to consider the magnitudes of these interactions as variable parameters which can significantly influence the electronic structure within the same layered perovskite "214" structure. La_2CuO_4 is particularly well known as the parent compound of a hole-doped high-T_c superconductor family in close proximity to a Mott-insulator ground state with antiferromagnetic ordering [1]. While Sr_2RuO_4 has the same crystal symmetry, its exotic low-T_c superconducting state emerges from a Fermi-liquid metallic state [2]. Its $5d$ counterpart Sr_2IrO_4 represents, in turn, a prototype spin-orbit Mott insulator [3–5]. In the presence of strong SOC, the three t_{2g} states of the Ir^{4+} ions with $5d^5$ electron configuration form bands described by the effective quantum numbers $J_{\text{eff}} = 3/2$ and $J_{\text{eff}} = 1/2$. The latter, which is half filled, is split already by moderate U into a lower and upper Hubbard band, opening the spin-orbit Mott gap.

The magnetic interactions in Sr_2IrO_4 also bear a resemblance to those in La_2CuO_4 and can be described within an antiferromagnetic Heisenberg model with an effective spin $1/2$ on a quasi-two-dimensional square lattice [5]. The discovery of a low-temperature d-wave gap [6,7] and a splitting of the Fermi surface into so-called separated Fermi arcs [8] in electron-doped Sr_2IrO_4, which are hallmarks of the doped cuprates [9], have recently been reported. These findings underscore the similarity of the the low-energy effective physics of Sr_2IrO_4 and that of the superconducting cuprates, and they encourage further research to elucidate the relationship between Mott physics and superconductivity and to search for new routes to high-T_c superconductivity.

Infrared and optical spectroscopies provide valuable information about the low-energy excitations, charge dynamics, and electron correlations in this class of materials. The in-plane conductivity spectra of single crystals of Sr_2IrO_4 have been systematically studied [10–12] and show evidence of the co-operative electron correlation and SOC effects in the presence of the orbital-dependent electron-phonon interaction. To make further inferences about the electronic structure and underlying interactions in the layered iridate Sr_2IrO_4, the interplane response needs to be carefully examined; likewise in the ruthenates and cuprates [13–20], where valuable information about the interplane coupling, phonon anomalies, pseudogap phase, and precursor Cooper-pair formation has been drawn from studies of the interlayer electrodynamics.

Furthermore, c-axis optical conductivity data, along with the in-plane spectra, can be used to significantly constrain the model parameters for band structure calculations, such as the on-site Coulomb interaction U.

A thorough and reliable study of the interplane response is impeded by the small size of the currently available crystals along the c axis, orthogonal to the IrO_2 planes. The interplane optical conductivity measured on a-axis-oriented Sr_2IrO_4 epitaxial films [21] is obscured by the substrate contribution and by the distorted electronic structure caused by the anisotropic biaxial strains [22,23]. Instead, we have used an array of high-quality and well-aligned Sr_2IrO_4 single crystals stacked along the c axis.

In this paper, we report a comprehensive ellipsometric study of the dielectric function anisotropy of Sr_2IrO_4 over a wide range of photon energies, extending from the far-infrared (far-IR) into the ultraviolet (UV), and its interpretation based on band structure and lattice dynamics calculations. The paper is organized as follows. Section II describes experimental and computational details. In Sec. III, the far-IR in- and out-of-plane phonon spectra are reported, followed by group theory analysis of the zone-center phonons and first-principles lattice dynamics calculations. The optical anisotropy of the interband transitions is discussed in Sec. IV. In Sec. V, relativistic calculations, which use the local spin-density approximation $+U$ (LSDA$+U$) approach to account for the on-site Coulomb interaction U simultaneously with strong spin-orbit coupling, are reported in order to explain the observed anomalies and

the anisotropy of the optical response. Finally, our conclusions are summarized in Sec. VI.

II. EXPERIMENTAL AND COMPUTATIONAL DETAILS

High-quality single crystals of Sr_2IrO_4 were grown by a self-flux method following Ref. [24]. They crystallize in the K_2NiF_4 structure with lattice parameters $a \approx 5.49$ Å and $c \approx 25.83$ Å. The platelike crystals mechanically extracted from the crucible had lateral dimensions of about 1.5×2 mm^2 in the ab plane and thicknesses less than 100 μm in the c direction. In order to gain a sample thickness along the c axis that is sufficient for optical spectroscopy, we prepared stacks of about 10 to 15 individual single crystals glued on top of each other by a minimal amount of GE varnish. The crystals were coaligned according to their in-plane crystallographic axes using Laue x-ray backscattering. Subsequently, one ac face of the stack was polished with dry polishing paper. The in-plane optical data were obtained from individual freshly cleaved as-grown platelike crystals.

We report spectroscopic ellipsometric data in a wide energy range from 12 meV to 6 eV over temperatures $T = 10$ to 300 K. For the IR range, we used home-built ellipsometers in combination with Bruker IFS 66v/S and Vertex 80v Fourier Transform IR spectrometers. Some of the experiments were performed at the infrared beam line IR1 of the ANKA synchrotron light source at Karlsruhe Institute of Technology, Germany [25]. Spectra in the visible and UV range were measured with a variable-angle spectroscopic ellipsometer (VASE, J. A. Woollam Co., Inc.) equipped with an ultrahigh vacuum cold-finger cryostat. The spectra were taken at different angles of incidence θ in the range of 65° to 75° for different spectral ranges.

Spectroscopic ellipsometry determines the complex reflectance ratio [26,27],

$$\rho = \frac{r_{pp}}{r_{ss}} = \tan\Psi e^{i\Delta}, \tag{1}$$

where r_{pp} and r_{ss} denote the reflectance of p and s polarized light and are given by the Fresnel equations, from which the full dielectric response $\varepsilon(\omega)$ is extracted.

For the calculations, we used the low-temperature experimental structural data according to Ref. [28]. To calculate the phonon spectrum, we employed scalar relativistic density functional perturbation theory [29] as implemented in QUANTUM ESPRESSO [30]. We used ultrasoft pseudopotentials [31], the generalized gradient approximation [32], and set the wave-function (charge density) plane-wave cutoff to 80 Ry (960 Ry), respectively. The initial structure was optimized to have a stress below 0.1 kbar and residual forces per atom smaller than 0.1 mRy/Bohr prior to the lattice dynamics calculation.

The relativistic band structure calculations were performed within the local spin-density approximation (LSDA) using the linear muffin-tin orbital (LMTO) method [33,34]. The Coulomb interaction of Ir $5d$ electrons in the presence of strong SOC was taken into account using the rotationally invariant LSDA+U method [35,36]. The on-site Coulomb repulsion U was varied in the range from 1.15 to 2.15 eV and Hunds coupling $J_H = 0.65$ eV was fixed to the value
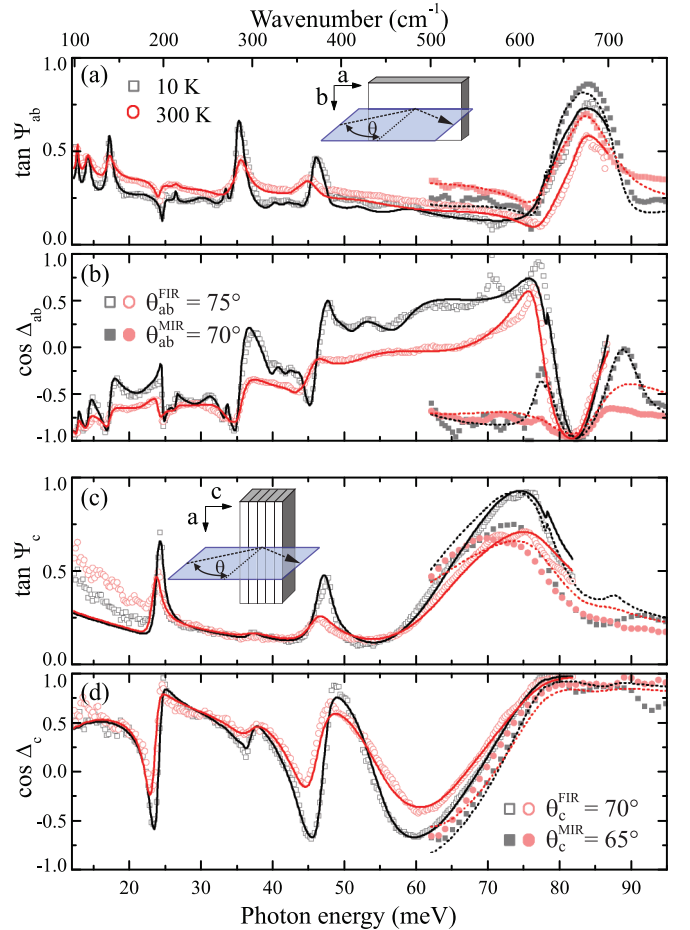

FIG. 1. Ellipsometric angles $\tan\Psi$ and $\cos\Delta$ in the far-infrared spectral range measured on (a), (b) the ab plane and (c), (d) the ac plane, with the c axis aligned in the plane of light incidence at $T = 10$ K (gray) and $T = 300$ K (red). The sketches in (a) and (c) illustrate the reflection geometry with respect to the crystallographic axes and plane of light incidence (blue). Empty and filled symbols denote measurements at different angles of incidence θ. Solid and dashed lines are the results of the fit to a model of multiple harmonic oscillators with Lorentzian line shapes.

estimated from LSDA. Thus, the parameter $U_{eff} = U - J_H$, which crudely determines the splitting between the lower and upper Hubbard bands, varied between 0.5 and 1.5 eV. The interband contribution to the imaginary part of the dielectric tensor was calculated using the dipole approximation to the matrix elements of the momentum operator [34]. Then, the real part was obtained using Kramers-Kronig transformation. Since the calculated optical conductivity does not show any significant dependence on the actual spin orientation within the antiferromagnetic phase, we assumed collinear antiferromagnetic order in the ab plane with Ir moments aligned along the c axis.

III. PHONON SPECTRUM

Figures 1(a) and 1(b) show the ellipsometric angles $\tan\Psi(\omega,\theta,T)$ and $\cos\Delta(\omega,\theta,T)$ obtained from the ab plane in the far-IR and mid-IR spectral range up to 95 meV (766 cm^{-1}). Figures 1(c) and 1(d) exhibit the corresponding ac-plane

response, where the c axis was coaligned with the plane of incidence as sketched in Figs. 1(a) and 1(c). Far-IR (empty symbols) and mid-IR (filled symbols) data were taken at different angles of incidence θ and overlap in the spectral range from 500 to 690 cm^{-1}. While there is certainly a finite spread in the alignment of individual single crystals of the stacks prepared for the c-axis measurements, there is no significant direct "contamination" from the in-plane response into the out-of-plane response due to misalignment, as already evident from the raw data. For instance, there is no significant absorption in the ac plane at the position of the highest-energy ab-plane feature around 664 cm^{-1}. This underlines the validity of our stacking approach.

In the case of a system with uniaxial anisotropy, the dielectric tensor $\varepsilon(\omega)$ has two complex eigenvalues, $\varepsilon^{ab}(\omega)$ and $\varepsilon^{c}(\omega)$. In principle, two independent ellipsometric data sets on ab and ac faces, as presented here, allow for wavelength-by-wavelength numerical inversion of the corresponding Fresnel equations [27]. However, due to numerical instability of the inversion process wherever $\tan \Psi$ and $\cos \Delta$ approach their extreme values of $[0,1]$ and ± 1, respectively, which happens especially around sharp spectral features, we have fitted the full anisotropic data set at the same time by two sets of harmonic oscillators with Lorentzian line shapes:

$$\varepsilon^{ab,c}(\omega) = \varepsilon_1^{ab,c}(\omega) + i\varepsilon_2^{ab,c}(\omega)$$

$$= \varepsilon_\infty^{ab,c} + \sum_{j \in ab,c} \frac{\Delta\epsilon_j \Omega_j^2}{\Omega_j^2 - \omega^2 - i\omega\Gamma_j}, \qquad (2)$$

where $\Delta\varepsilon_j$, Ω_j, and Γ_j denote the oscillator strength, center frequency, and linewidth of the jth phonon resonance, respectively, and $\varepsilon_\infty^{ab,c}$ is the effectively constant contribution of the high-energy interband transitions to the real part of the dielectric function in the far-IR range. For the highest-energy c-axis phonon at 515 cm^{-1}, we have to use a Voigt profile (that is, a Lorentzian profile broadened by convolution with a Gaussian with width Γ_{Gauss}) to account for the anomalously large linewidth. This additional broadening might be caused by the stacking approach and polishing of the crystal stack. The results of the corresponding fits are shown as solid lines in Fig. 1 for temperatures $T = 10$ and 300 K, respectively. Accordingly, the fitted complex dielectric response is shown in Fig. 2 for both the ab plane and the c axis also for intermediate temperatures. The best-fit parameters for $T = 10$ K are summarized in Table I along with the ab-plane results from Moon *et al.* [11], where we find good agreement.

We unambiguously distinguish eight phonon resonances in the ab plane and four in the c-axis dielectric response in contrast to six in-plane modes reported so far [11]. The double-peak structure located at 324 and 339 cm^{-1} develops at low temperatures only and might be related to two additional phonons. It can be clearly seen in the spectra presented by Moon *et al.* [11], but is not discussed there. Thus, in total, we identify ten in-plane phonon modes. The dip feature at 200 cm^{-1} clearly seen in the raw data of the in-plane response is a result of the ellipsometric measurement scheme and correctly modeled and reproduced by the lowest-energy c-axis phonon at 192 cm^{-1}. While the ab-plane phonons exhibit a small linewidth Γ_j, indicating a high single-crystal quality, all
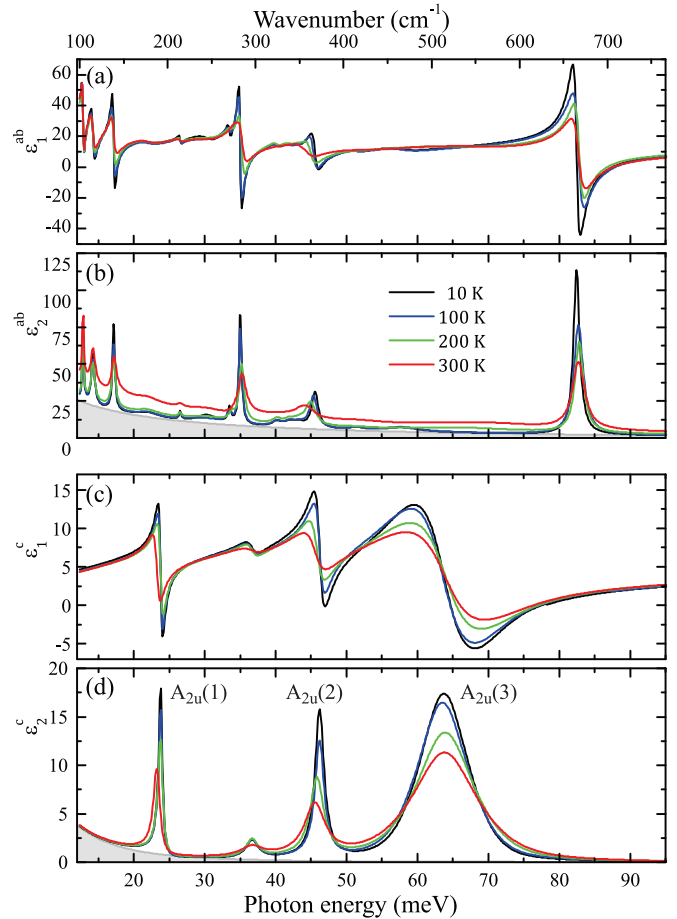

FIG. 2. Fitted far-infrared phonon spectra. Real parts of the optical conductivity σ_1 and permittivity ε_1 for (a), (b) the ab plane and (c), (d) the c-axis response, respectively, at selected temperatures.

four c-axis resonances are considerably broader. This might be attributed to the stacking procedure of many single crystals with enhanced contribution of the near-surface regions of the individual crystals inside the stack into the c-axis optical response. Mechanical polishing as applied here can also induce strain effects and defects which can increase the apparent phonon linewidth [37,38].

We find, for both in- and out-of-plane response, a nonzero background of absorption, which can be attributed to oxygen deficiency in the crystals [39]. This might indeed have occurred under the growth conditions applied here. This background is modeled by a broad Lorentzian and shown as a shaded area for the $T = 10$ K case in Fig. 2. It shows moderate temperature dependence only between $T = 200$ and 300 K.

The temperature dependence of the resonant frequencies Ω_j and corresponding linewidths Γ_j for a representative set of in-plane and all out-of-plane modes is shown in Figs. 3(a)–3(d). The resonance frequencies of the in-plane modes reproduce the reported behavior [11] and the out-of-plane modes show qualitatively similar characteristics: a regular anharmonic softening by 1.5% at 300 K of the modes at 192 and 373 cm^{-1}, whereas the other two exhibit a small hardening upon heating. For the c-axis modes, as expected from the already enhanced linewidth at low temperatures, the increase of Γ_j with rising temperature is only moderate compared to their in-plane counterparts.

TABLE I. Best-fit results for the phonon resonances in the far-IR spectral range of Sr_2IrO_4 at $T = 10$ K with $\Omega_j, \Delta\varepsilon_j, \Gamma_j$ being the resonance frequency, the contribution to the static permittivity, and linewidth, respectively, according to the Lorentz oscillator model. And the resonance frequencies Ω_j^{calc} of the IR-active optical zone-center phonons of E_u and A_{2u} symmetry from first-principles lattice dynamics calculations. p characterizes the atomic displacements along the c axis, as described in the main text.

Experiment				Calculation	
Ω_j (cm^{-1})	$\Delta\varepsilon_j$	Γ_j (cm^{-1})	$\Omega_j{}^a$ (cm^{-1})	Ω_j^{calc} (cm^{-1})	p
ab plane				E_u	
103	1	2.1	102	30	0.21
115	1.33	4.4	116	81	0.08
138	1.31	2.9	137	92	0.09
214	0.07	2.7		122	0.03
270	0.17	4.4		178	0.10
282.5	0.93	3.3	284	186	0.03
324	0.13	13	322	212	0.21
339	0.17	16	338	251	0.01
367	0.57	8.8	366	298	0.15
664	1.43	8.6	663	323	0.56
				406	0.00
				645	0.00
c axis				A_{2u}	
192	0.46	5.2		172	1.00
296	0.11	17		374	1.00
373	0.53	13		443	1.00
515	2.6	10^b		660	0.00

^{a}Reference [11].
$^b\Gamma_{Gauss} = 24$ cm^{-1}.

A space-group analysis helps us to crosscheck our findings. The space group $I4_1/acd$ with the Wyckoff positions for Ir (8a), Sr (16d), and the two different oxygen sites (apical 16d
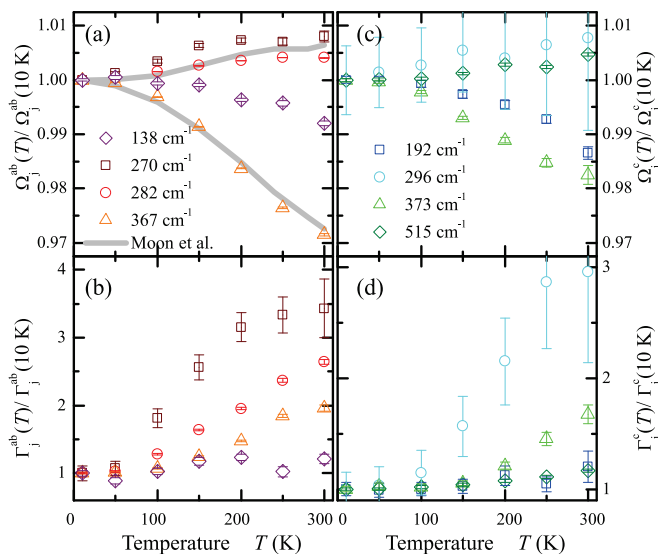

FIG. 3. Temperature-dependent phonon parameters of Sr_2IrO_4 normalized to $T = 10$ K. (a), (c) Normalized resonance frequencies Ω_j and (b), (d) linewidth Γ_j for *ab*-plane and *c*-axis response, respectively. The gray lines in (a) are reproduced from Ref. [11].

and basal 16f) [40] allows four A_{2u} and 12 doubly degenerate E_u infrared active optical phonons [41]. All modes belonging to the same irreducible representation (here either A_{2u} or E_u) are allowed to mix in order to form the eigenmodes that embody atomic displacements in both in- and out-of-plane directions. The symmetry of a tetragonal crystal in $I4_1/acd$ restricts the A_{2u} (E_u) modes to be excited only by an electric field, which is polarized along the c axis (*ab* plane), since the net in-plane (out-of-plane) dipole moments cancel out perfectly within one unit cell. To assign with particular eigen-patterns, we compare our experimentally extracted phonon parameters with results from lattice dynamics calculations. The set of calculated zone-center phonon eigenfrequencies is summarized in the right side of Table I. Since in our density functional theory (DFT) calculation Sr_2IrO_4 is metallic, the Born effective charges are not available (and therefore the oscillator strength). As an alternative, we judge the atomic displacements of each of the phonon eigenmodes by the quantity p, which is the norm of the projections of the normalized eigenvector onto the *ab* plane and c axis (see the Appendix). The respective values of p are also listed in Table I. If $p = 0$, all atoms are displaced only within the *ab* plane; for $p = 1$, all atoms are displaced purely along the c axis. Although p is not proportional to the true oscillator strength, due to the symmetry of the tetragonal $I4_1/acd$ structure, we can take p as a zeroth-order approximation of the relative oscillator strength (see Appendix), i.e., for A_{2u} (E_u), we can expect modes with $p = 1$ ($p = 0$) to be stronger than modes with $p = 0$ ($p = 1$).

According to the calculated eigenvectors, we find that the set of four A_{2u} modes actually consists of three with almost pure c-axis displacements and one with almost pure displacements within the *ab* plane. The respective mode patterns are depicted in Fig. 4. The c-axis modes $A_{2u}(1)$ to $A_{2u}(3)$ lead to octahedron bending and oscillations of the IrO_6 octahedra against the Sr ions, well known from the high-symmetry structure $I4/mmm$ [42]. $A_{2u}(4)$, however, predominantly involves the planar oxygen atoms and leads to a quasiquadrupolar mode, which stems from the backfolding of zone boundary modes (from the M point of the high-symmetry structure $I4/mmm$) due to the rotation of the octahedra and concomitant enlargement of the unit cell. Within the calculation, the displacements of the Ir and O along the c axis are four order of magnitudes smaller than the in-plane
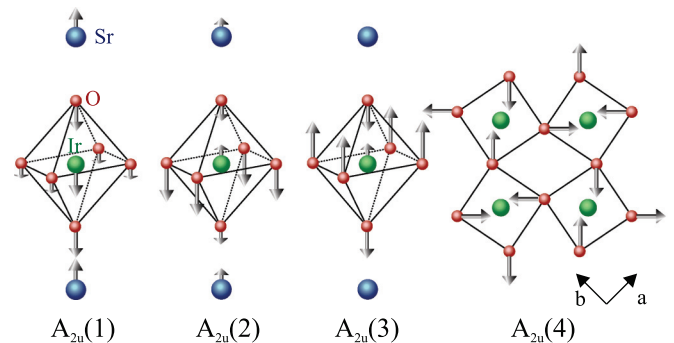

FIG. 4. Calculated eigenvectors of the infrared-active optical phonon modes with A_{2u} symmetry at the Γ point of the $I4_1/acd$ structure.
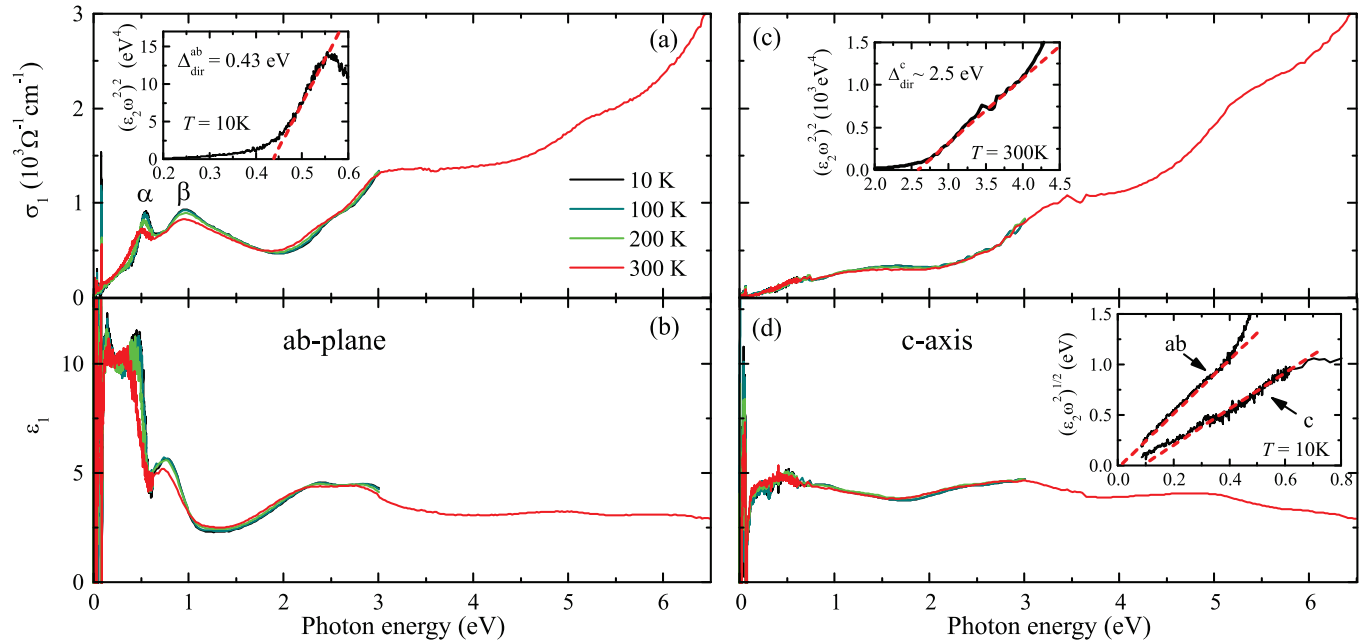
FIG. 5. Temperature dependence of the real parts of the optical conductivity σ_1 and dielectric permittivity ε_1 of Sr_2IrO_4 in the spectral range of 0.01 to 6.5 eV. (a), (b) ab-plane and (c), (d) c-axis optical response. α and β denote the low-energy interband transitions into unoccupied $J_{\text{eff}} = 1/2$ states from $J_{\text{eff}} = 1/2$ and $J_{\text{eff}} = 3/2$ initial states, respectively. Insets: (a) In-plane direct optical gap $\Delta_{\text{dir}}^{ab} = 0.43$ eV and (c) out-of-plane absorption edge $\Delta_{\text{dir}}^c = 2.5$ eV, respectively, extracted from $(\varepsilon_2\omega^2)^2$, (d) ab-plane and c-axis low-energy optical response $(\varepsilon_2\omega^2)^{1/2}$ and inferred indirect optical gaps.

displacements, hence $p = 0.00$. Since there is no out-of-plane tilting, one expects the change in the macroscopic polarization from this in-plane displacement to be small. Thus we expect three resonances in the c-axis response. In our experimental data, we find three strong and well-defined modes at 192, 373, and 515 cm^{-1}, which we assign to $A_{2u}(1)$ to $A_{2u}(3)$. The weak mode which is clearly detected at 296 cm^{-1} cannot be assigned to $A_{2u}(4)$ since it is too low in energy. We therefore consider an in-plane E_u mode to show up here. If the crystal symmetry is broken locally, e.g., around defects, the perfect cancellation of c-axis displacements is lifted and modes, which possess E_u symmetry in bulk, might be excited by an electric field along the c axis, too. E_u modes with large c-axis displacements are most susceptible to these distortions, while others with $p = 0$ remain silent. Within our calculation, we find indeed one mode at 323 cm^{-1} with $p = 0.56$, which tilts the IrO_6 octahedra, as an excellent candidate.

With the highest in-plane phonon frequency at 645 cm^{-1}, the full frequency range of the calculation matches quite well with the experimental one (664 cm^{-1}). In qualitative agreement with the experimental results, we also find the highest detectable c-axis phonon at considerably lower frequency (expt: 515 cm^{-1}; calc: 443 cm^{-1}) compared to the in-plane modes. The sizable numerical discrepancy between the calculated and measured phonon frequencies is probably due to the fact that the material is metallic in this lattice dynamics calculation. The phonon frequencies are therefore affected by charge screening, which is not present in the insulating compound.

In summary, following this analysis and in contrast to previous work [12,43], we assign the experimental c-axis modes at 192, 373, and 515 cm^{-1} to be the one of A_{2u} symmetry,

and the one at 296 cm^{-1} to be an impurity mode (derived from an E_u mode) originating from local symmetry breaking near the defect regions (sample stack). The in-plane modes are of E_u symmetry solely. The far-infrared phonon spectrum is consistent with group symmetry considerations and lattice dynamics calculations. Distinct in- and out-of-plane spectra prove that the sample stack can be considered as an almost quasisingle domain in terms of its optical response, which allows us to examine the anisotropic dielectric tensor also at higher photon energies.

IV. OPTICAL ANISOTROPY

Figure 5 shows the real parts of the dielectric function and optical conductivity in plane ($\varepsilon_{a,1}$ and $\sigma_{a,1}$) as well as out of plane ($\varepsilon_{c,1}$ and $\sigma_{c,1}$) in the photon energy range from 0.01 to 6.5 eV. Since $\tan\Psi$ and $\cos\Delta$ are far from their extrema, we apply the numerical inversion to correct for the anisotropy. In this energy range, only moderate corrections to the absolute values of ε are introduced.

First, we will focus on the in-plane response at photon energies up to 6.5 eV. The measured spectra agree very well with the spectra previously reported in the spectral range up to 3 eV by Moon $et~al.$ [11] and Sohn $et~al.$ [12]. We assign the low-energy interband transitions accordingly as α and β. Above 2 eV, we find strong absorption setting in due to interband transitions with a plateaulike feature around 3 eV and a further increase at higher photon energies with another shoulder around 5.5 eV.

Following Fermi's golden rule, one finds the following frequency dependence of the imaginary part of the dielectric constant $\varepsilon_2(\omega)$ for photon energies just above the direct optical

gap Δ_{dir} [44,45]: $\varepsilon_2(\omega) \propto \omega^{-2}[\hbar\omega - \Delta_{dir}]^{1/2}$. Therefore, we plot $(\varepsilon_2\omega^2)^2$ in the inset of Fig. 5(a) and obtain $\Delta_{dir}^{ab} = 0.43$ eV at $T = 10$ K from the linear fit. Both the amplitude and the temperature dependence of the gap are in good agreement with the reported values [11].

The out-of-plane response, however, shows remarkably different behavior. While at high photon energies the optical conductivity is almost identical to the in-plane response with very similar characteristic shoulder features around 3 and 5 eV, the two bands α and β at lower photon energies are strongly suppressed with a remaining broad, humplike background extending down to low frequencies. As illustrated in the inset of Fig. 5(c), the main absorption edge setting in at 2.5 eV indeed shows the signature of a direct transition. Surprisingly, the temperature dependence of the c-axis response is rather weak up to room temperature. The low-energy optical response can be understood in terms of an indirect gap. Phonon-assisted absorption across an indirect optical gap involves essentially two processes. When the photon is absorbed, an additional phonon can either be absorbed or emitted in order to fulfill energy and momentum conservation conditions. While the former strongly depends on the phonon density and is therefore strongly suppressed at low temperatures, the latter is much stronger and only weakly temperature dependent. For an indirect gap of two parabolic bands, one expects [45] $\varepsilon_2(\omega) \propto \omega^{-2}(\hbar\omega \pm \hbar\Omega_{ph} - \Delta_{indir})^2$. As depicted in the inset of Fig. 5(d), this expression provides a reasonable description of the experimental data for both the ab-plane and c-axis response. The linear fit to the low-energy tail of the direct gap in the ab response extrapolates to about 10–20 meV and the c-axis response to a range of 50–100 meV. With uncertainty of the emitted phonon modes, we estimate Δ_{ind} to several tens of meV.

A similar trend has recently been reported on thin films of Sr_2IrO_4 epitaxially grown along the $\langle 110 \rangle$ direction on $LaSrGaO_4$ (100) substrates, which also provides access to the c-axis response by normal incidence transmission [21]. Although lattice mismatch and inevitable biaxial strain effects lead to a significant orthorhombic distortion and hence a shift in the α and β bands to lower energies, the main features—strong suppression of α and β followed by an upturn and shoulder around 3 eV—are quite similar in both sets of materials.

In an ionic picture, the origin of the optical anisotropy with respect to the α and β interband transitions might be attributed to intersite hopping of the excited electrons since on-site $d - d$ transitions are forbidden by the dipole selection rules [21], but this picture neglects the spatially extended nature and hybridization of the $5d$ valence states, as evident from the relatively large electronic bandwidths W realized in $5d$ TMOs. To elucidate the complex pattern of interband transitions and optical gaps, we compare our experimental results with the optical conductivity from electronic band structure calculations.

V. BAND STRUCTURE CALCULATIONS

The electronic band structure in the energy range of -8 to 8 eV and an expansion of the region around the Fermi energy $[-1.5 eV, 1 eV]$ are depicted in Figs. 6(a) and 6(b), respectively. In Fig. 6(b), the bands are decorated with circles
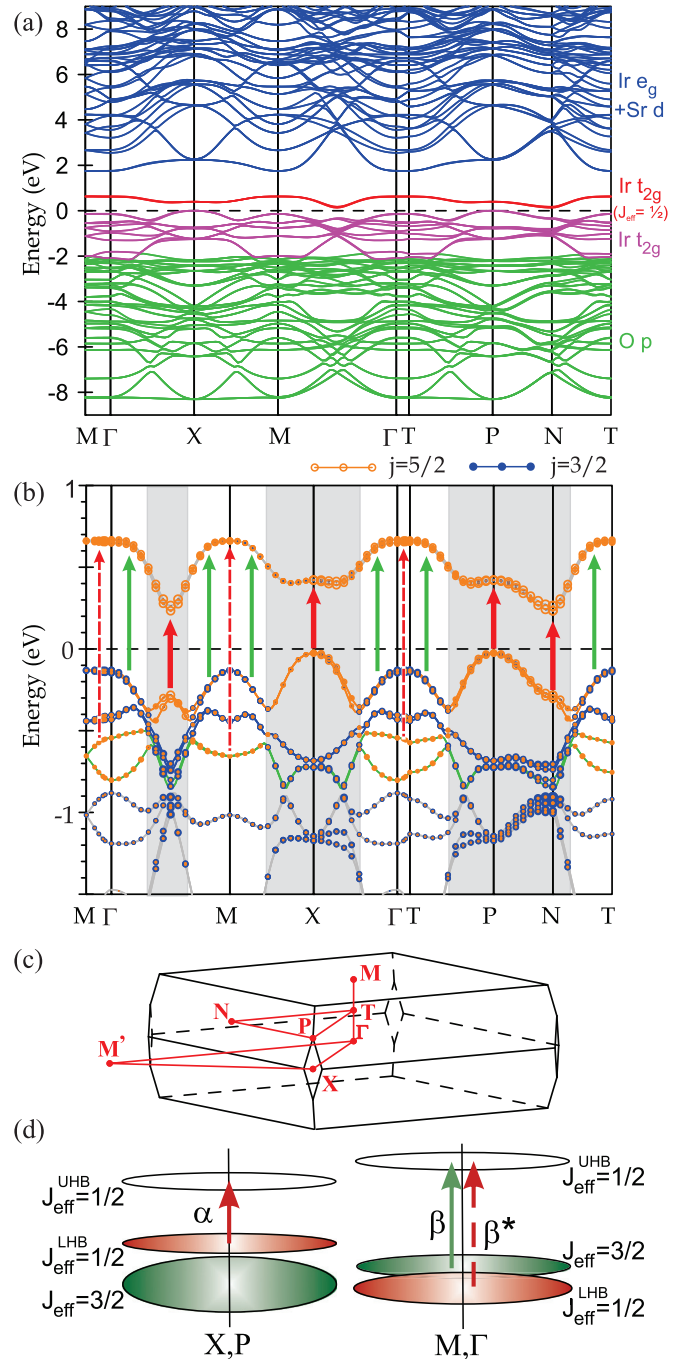

FIG. 6. (a) Electronic band structure and respective dominant orbital character from LSDA+U calculations with $U_{eff} = 1.3$ eV. Colors represent dominant orbital character as in the legend. (b) Enlargement of the band structure in (a). The size of the blue and orange circles is proportional to the weight of the orbital character when projected onto $d_{3/2}$ and $d_{5/2}$ states, respectively. The red and green arrows indicate $J_{eff} = 1/2 \rightarrow J_{eff} = 1/2$ and $J_{eff} = 3/2 \rightarrow J_{eff} = 1/2$, respectively. (c) Brillouin zone of $I4_1/acd$. (d) Sketch of the main contributions to the low-energy α, β double-peak structure.

proportional in size to their orbital character projected onto the basis set of Ir $d_{3/2}$ (blue) and $d_{5/2}$ (orange) states. In the basis of eigenfunctions of the "true" total angular momentum j, the functions of the $J_{eff} = 3/2$ quartet are dominated by $d_{3/2}$ states with some minor weight of $d_{5/2}$ ones, which is determined by
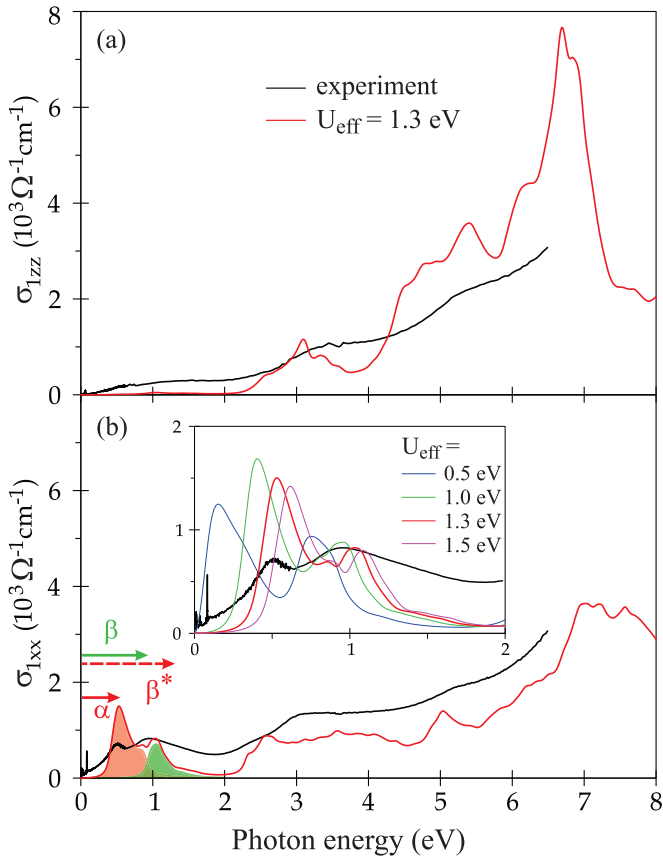
FIG. 7. Calculated (a) out-of-plane and (b) in-plane optical conductivity $\sigma_{1,zz}$ and $\sigma_{1,xx}$, respectively, along with the experimental spectra at $T = 300$ K. The shaded areas denote the contributions to the α and β interband transitions. Inset: Near-infrared in-plane double-peak structure for different values of on-site repulsion U_{eff}. $U_{eff} = 1.3$ eV is chosen to match the position of the peaks.

the relative strengths of SOC and crystal-field splitting. The $J_{eff} = 1/2$ functions, on the other hand, are given by linear combinations of $d_{5/2}$ states only. This allows one to identify bands with pure $d_{5/2}$ character as originating from $J_{eff} = 1/2$ states. As expected, we find the upper Hubbard band with pure $d_{5/2}$, i.e., $J_{eff} = 1/2$, character well separated from the lower $J_{eff} = 1/2$ Hubbard band and the $J_{eff} = 3/2$ states below the Fermi level [red and purple lines in Fig. 6(a)]. We adjusted U_{eff} to match the position of the low-energy α and β transitions [inset of Fig. 7]. Hence, the direct optical band gap is naturally found to be about 0.4 eV in our calculations.

Before we discuss the high-energy features, we will focus on the analysis of the low-energy α and β double-peak structure of the in-plane response. The α band indeed stems from transitions between initial and final bands formed by pure $J_{eff} = 1/2$ states, but only from restricted sections of the **k** space near zone boundaries, e.g., around the X point or the $P - N$ high-symmetry line [solid red arrows and gray shaded areas in Fig. 6(b)]. The antiferromagnetic order of the Ir moments within the ab plane stabilized by the on-site Coulomb repulsion U causes opening of a gap near the zone boundary between two pairs of bands which are nearly degenerate in non-spin-polarized relativistic LDA calculations. These two pairs of bands show nearly parallel dispersions which

insures a high joint density of states for interband transitions responsible for the α band. This is in line with both previous theoretical dynamical mean-field [46] and experimental photoemission [47] results. Both find the highest occupied states with $J_{eff} = 1/2$ character around the X point, too.

The β band located around 1 eV, however, is more intricate. The occupied $J_{eff} = 1/2$ bands exhibit rather strong dispersion with the total width of about 0.8 eV. They cross the $J_{eff} = 3/2$ bands so that near the Brillouin-zone center along the $\Gamma - T - M$ line, the bottom of the $J_{eff} = 1/2$ bands is buried well below the top of the $J_{eff} = 3/2$ ones. In agreement with previous results [3,46], we found the β band to have a dominant contribution from transitions with $J_{eff} = 3/2$ initial states [green arrows]. However, in contrast to the previous interpretation based on a simplified band picture [3], transitions from $J_{eff} = 1/2$ initial bands also contribute to the optical conductivity at ~1.2 eV (dashed red arrows). While the dynamical mean-field theory results [46] lead to the same conclusions, Kim *et al.* [48] favor an interpretation in terms of a Fano-type interference of the broad $J_{eff} = 1/2$ electron-hole continuum with an optically inactive so-called SO exciton, i.e., a magnetically active mode found as a broad peak around 0.7 eV in resonant inelastic x-ray experiments [5,49]. This depletes the optical excitation spectrum in that energy range which leaves the two-peak structure. Our calculations give the lower α band about twice as strong as the higher β band, while in the experimental spectra, the strength is approximately the same for both. Kim *et al.* [48] observed a similar trend in their microscopic model calculations when considering clusters of four Ir ions. They relate this to interband mixing of $J_{eff} = 3/2$ and $J_{eff} = 1/2$ states, which reflects the itinerancy of the system, i.e., the hybridization of Ir d states via neighboring oxygen $2p$ states.

Furthermore, our calculations allow us to analyze the full anisotropic optical response up to high energies. Figures 7(a) and 7(b) present the real parts of the calculated optical conductivity $\sigma_{1,zz}$ (out of plane) and $\sigma_{1,xx}$ (in plane) in the spectral range up to 8 eV along with the experimental data taken at $T = 300$ K.

Most noticeable is the large optical gap of about 2.2 eV along the c axis [Fig. 7(a)], followed by a weak band centered around 3 eV and several stronger bands around 5.5 and 7 eV, in rather good overall agreement with the experimentally obtained c-axis response. For α and β, we find the dipole matrix elements for c-axis polarization below 2 eV either completely vanishing as for the $J_{eff} = 1/2 \rightarrow J_{eff} = 1/2$ transitions, or for $J_{eff} = 3/2 \rightarrow J_{eff} = 1/2$ to be strongly suppressed in strength by roughly two orders of magnitude compared to the in-plane response. Above 2 eV, interband transitions from the low-lying oxygen p states into the unoccupied $J_{eff} = 1/2$ states set in. This matches the absorption edge we find in the out-of-plane response around 2.5 eV.

In the in-plane response [Fig. 7(b)], we identify three major features. Besides the discussed double-peak structure, the next set of interband transitions sets in around 2.2 eV, concurrent with the c-axis response but at somewhat lower frequency than in the experimental spectra. From there, a plateau reaches out to about 5 eV followed by a further rise peaking at 7 eV with approximately half the strength of the c-axis response. The

weak feature around 5.2 eV seen in the experiment might find its counterpart at 5 eV in the calculation.

Along the Brillouin-zone boundaries, for example between the P and N points (see Fig. 6), we find an indirect optical gap of about 0.2 eV. This could indeed enable phonon-mediated indirect transitions, which as second-order processes are beyond our calculations. These transitions may contribute to the hump in the c-axis response as well as the strongly temperature-dependent absorption edge tail and far-IR background seen in the ab plane. The latter has also been shown to be relevant to $Sr_3Ir_2O_7$, the narrow band-gap bilayer analogue [50].

VI. CONCLUSIONS

We demonstrate the feasibility of a stacking approach of single crystals to extract the c-axis optical conductivity of Sr_2IrO_4 as proven by a distinct phonon spectrum, which is in full accordance with lattice dynamics calculations. The observed uniaxial anisotropy in the infrared excitation spectrum is consistent with the suggested $J_{eff} = 1/2$ ground state within the LSDA+U band structure calculations. The absence of the characteristic IR double-peak structure in the out-of-plane response is explained by vanishing dipole matrix elements. Our comprehensive investigation of the optical response of a prototypical spin-orbit Mott insulator thus provides an excellent basis for experiments on doped layered iridates, which are promising candidates for exotic ground states including unconventional superconductivity.

APPENDIX: RELATION BETWEEN IR CROSS SECTION AND PROJECTION p

The oscillator strength or IR cross section IR_i^α of the ith phonon eigenmode u_i with respect to an applied electric field (IR radiation) polarized along the $\alpha = [x,y,z]$ direction is given by

$$IR_i^\alpha = A \left[\sum_{j=1, n=1}^{3, N_{atom}} u_{i,(3n-3+j)} Z_{j,n}^{*\alpha} \right]^2, \quad (A1)$$

where $Z_{j,n}^{*\alpha}$ is the Born effective charge tensor of the atom n within the unit cell and A is a constant. $Z_{j,n}^{*\alpha}$ describes the change in polarization in direction α with respect to a displacement of atom n along the Cartesian direction j. Since Sr_2IrO_4 is metallic in DFT, $Z_{j,n}^{*\alpha}$ is not accessible. However, based on the fact that the induced polarization in Sr_2IrO_4 is not necessarily parallel to the atomic displacement, we use a simplified formula to qualitatively judge the IR cross section:

$$p = 0.5 + 0.5(e_c - e_{ab}), \quad (A2)$$

with

$$e_{ab} = \sum_{n, j=x, y}^{N_{atom}} |u_{i,(3n-3+j)}|^2, \quad e_c = \sum_{n, j=z}^{N_{atom}} |u_{i,(3n-3+j)}|^2.$$

The quantity p is the projection of the atomic displacement u_i onto the crystal axes. Since the u_i's are normalized, $p = 0$ if the mode is purely in plane and $p = 1$ if the mode is out of plane. Comparing Eq. (A1) to Eq. (A2), we note that p is not directly proportional to IR_i^α, but it qualitatively catches the diagonal and off-diagonal elements of $Z_{j,n}^{*\alpha}$. The symmetry of $Z_{j,n}^{*\alpha}$ depends on the space group. In cubic systems, for instance, $Z_{j,n}^{*\alpha}$ is diagonal. In Sr_2IrO_4 with $I4_1/acd$ symmetry, $Z_{x/y}^{*z}$ is not forced to be zero for the O $16f$ site, i.e., the macroscopic polarization along the z axis can change with an in-plane displacement, and vice versa. If the distortions from tetragonal site symmetry are not too large, these off-diagonal components should be noticeably smaller than the diagonal ones. Thus, in zeroth order, $IR_i^j \propto |u_{i,3n-3+j}|^2$, i.e., the atomic displacement and the dipole moment point in the same direction. For this reason, the cross section of the $A_{2u}(4)$ mode with mainly in-plane displacements ($p \approx 0$) should be considerably smaller than the cross section of the modes with out-of-plane displacements ($p \approx 1$). Having this information at hand allows a more precise assignment of the modes as based exclusively on symmetry arguments. The respective argument is true for the E_u modes also.

[1] H. Takagi, Nat. Mater. **6**, 179 (2007).

[2] A. P. Mackenzie and Y. Maeno, Rev. Mod. Phys. **75**, 657 (2003).

[3] B. J. Kim, H. Jin, S. J. Moon, J.-Y. Kim, B.-G. Park, C. S. Leem, J. Yu, T. W. Noh, C. Kim, S.-J. Oh, J.-H. Park, V. Durairaj, G. Cao, and E. Rotenberg, Phys. Rev. Lett. **101**, 076402 (2008).

[4] B. J. Kim, H. Ohsumi, T. Komesu, S. Sakai, T. Morita, H. Takagi, and T. Arima, Science **323**, 1329 (2009).

[5] J. Kim, D. Casa, M. H. Upton, T. Gog, Y.-J. Kim, J. F. Mitchell, M. van Veenendaal, M. Daghofer, J. van den Brink, G. Khaliullin, and B. J. Kim, Phys. Rev. Lett. **108**, 177003 (2012).

[6] Y. K. Kim, N. H. Sung, J. D. Denlinger, and B. J. Kim, Nat. Phys. **12**, 37 (2016).

[7] Y. J. Yan, M. Q. Ren, H. C. Xu, B. P. Xie, R. Tao, H. Y. Choi, N. Lee, Y. J. Choi, T. Zhang, and D. L. Feng, Phys. Rev. X **5**, 041018 (2015).

[8] Y. K. Kim, O. Krupin, J. D. Denlinger, A. Bostwick, E. Rotenberg, Q. Zhao, J. F. Mitchell, J. W. Allen, and B. J. Kim, Science **345**, 187 (2014).

[9] B. Keimer, S. A. Kivelson, M. R. Norman, S. Uchida, and J. Zaanen, Nature (London) **518**, 179 (2015).

[10] S. J. Moon, H. Jin, K. W. Kim, W. S. Choi, Y. S. Lee, J. Yu, G. Cao, A. Sumi, H. Funakubo, C. Bernhard, and T. W. Noh, Phys. Rev. Lett. **101**, 226402 (2008).

[11] S. J. Moon, H. Jin, W. S. Choi, J. S. Lee, S. S. A. Seo, J. Yu, G. Cao, T. W. Noh, and Y. S. Lee, Phys. Rev. B **80**, 195110 (2009).

[12] C. H. Sohn, M.-C. Lee, H. J. Park, K. J. Noh, H. K. Yoo, S. J. Moon, K. W. Kim, T. F. Qi, G. Cao, D.-Y. Cho, and T. W. Noh, Phys. Rev. B **90**, 041105 (2014).

[13] T. Katsufuji, M. Kasai, and Y. Tokura, Phys. Rev. Lett. **76**, 126 (1996).

[14] K. Pucher, A. Loidl, N. Kikugawa, and Y. Maeno, Phys. Rev. B **68**, 214502 (2003).

[15] S. V. Dordevic, S. Komiya, Y. Ando, and D. N. Basov, Phys. Rev. Lett. **91**, 167401 (2003).

[16] A. A. Schafgans, A. D. LaForge, S. V. Dordevic, M. M. Qazilbash, W. J. Padilla, K. S. Burch, Z. Q. Li, S. Komiya, Y. Ando, and D. N. Basov, Phys. Rev. Lett. **104**, 157002 (2010).

[17] D. N. Basov and T. Timusk, Rev. Mod. Phys. **77**, 721 (2005).

[18] A. V. Boris, D. Munzar, N. N. Kovaleva, B. Liang, C. T. Lin, A. Dubroka, A. V. Pimenov, T. Holden, B. Keimer, Y.-L. Mathis, and C. Bernhard, Phys. Rev. Lett. **89**, 277001 (2002).

[19] L. Yu, D. Munzar, A. V. Boris, P. Yordanov, J. Chaloupka, T. Wolf, C. T. Lin, B. Keimer, and C. Bernhard, Phys. Rev. Lett. **100**, 177004 (2008).

[20] A. Dubroka, M. Rössle, K. W. Kim, V. K. Malik, D. Munzar, D. N. Basov, A. A. Schafgans, S. J. Moon, C. T. Lin, D. Haug, V. Hinkov, B. Keimer, T. Wolf, J. G. Storey, J. L. Tallon, and C. Bernhard, Phys. Rev. Lett. **106**, 047006 (2011).

[21] J. Nichols, O. B. Korneta, J. Terzic, L. E. De Long, G. Cao, J. W. Brill, and S. S. A. Seo, Appl. Phys. Lett. **103**, 131910 (2013).

[22] A. Lupascu, J. P. Clancy, H. Gretarsson, Z. Nie, J. Nichols, J. Terzic, G. Cao, S. S. A. Seo, Z. Islam, M. H. Upton, J. Kim, D. Casa, T. Gog, A. H. Said, V. M. Katukuri, H. Stoll, L. Hozoi, J. van den Brink, and Y.-J. Kim, Phys. Rev. Lett. **112**, 147201 (2014).

[23] C. Rayan Serrao, J. Liu, J. T. Heron, G. Singh-Bhalla, A. Yadav, S. J. Suresha, R. J. Paull, D. Yi, J.-H. Chu, M. Trassin, A. Vishwanath, E. Arenholz, C. Frontera, J. Železný, T. Jungwirth, X. Marti, and R. Ramesh, Phys. Rev. B **87**, 085121 (2013).

[24] G. Cao, J. Bolivar, S. McCall, J. E. Crow, and R. P. Guertin, Phys. Rev. B **57**, R11039 (1998).

[25] C. Bernhard, J. Humlíček, and B. Keimer, Thin Solid Films **455-456**, 143 (2004).

[26] H. Fujiwara, *Spectroscopic Ellipsometry* (Wiley, New York, 2007).

[27] R. M. A. Azzam and N. M. Bashara, *Ellipsometry and Polarized Light* (North-Holland, Amsterdam, 1977).

[28] T. Shimura, Y. Inaguma, T. Nakamura, M. Itoh, and Y. Morii, Phys. Rev. B **52**, 9143 (1995).

[29] S. Baroni, S. de Gironcoli, A. Dal Corso, and P. Giannozzi, Rev. Mod. Phys. **73**, 515 (2001).

[30] P. Giannozzi, S. Baroni, N. Bonini, M. Calandra, R. Car, C. Cavazzoni, D. Ceresoli, G. L. Chiarotti, M. Cococcioni, I. Dabo, A. D. Corso, S. de Gironcoli, S. Fabris, G. Fratesi, R. Gebauer, U. Gerstmann, C. Gougoussis, A. Kokalj, M. Lazzeri, L. Martin-Samos, N. Marzari, F. Mauri, R. Mazzarello, S. Paolini, A. Pasquarello, L. Paulatto, C. Sbraccia, S. Scandolo, G. Sclauzero, A. P. Seitsonen, A. Smogunov, P. Umari, and R. M. Wentzcovitch, J. Phys.: Condens. Matter **21**, 395502 (2009).

[31] We used the pseudopotentials Sr.pbe-nsp-van.UPF, Ir.pbe-n-rrkjus.UPF, and O.pbe-n-rrkjus.UPF from http://www.quantum-espresso.org.

[32] J. P. Perdew, K. Burke, and M. Ernzerhof, Phys. Rev. Lett. **77**, 3865 (1996).

[33] O. K. Andersen, Phys. Rev. B **12**, 3060 (1975).

[34] V. N. Antonov, B. N. Harmon, and A. N. Yaresko, *Electronic Structure and Magneto-Optical Properties of Solids* (Kluwer Academic, Dordrecht, 2004).

[35] A. I. Liechtenstein, V. I. Anisimov, and J. Zaanen, Phys. Rev. B **52**, R5467 (1995).

[36] A. N. Yaresko, V. N. Antonov, and P. Fulde, Phys. Rev. B **67**, 155103 (2003).

[37] D. J. Evans and S. Ushioda, Phys. Rev. B **9**, 1638 (1974).

[38] H. Shen and F. H. Pollak, Appl. Phys. Lett. **45**, 692 (1984).

[39] N. H. Sung, H. Gretarsson, D. Proepper, J. Porras, M. L. Tacon, A. V. Boris, B. Keimer, and B. J. Kim, Philos. Mag. **96**, 413 (2016).

[40] M. K. Crawford, M. A. Subramanian, R. L. Harlow, J. A. Fernandez-Baca, Z. R. Wang, and D. C. Johnston, Phys. Rev. B **49**, 9198 (1994).

[41] E. Kroumova, M. Aroyo, J. Perez-Mato, A. Kirov, C. Capillas, S. Ivantchev, and H. Wondratschek, Phase Trans. **76**, 155 (2003).

[42] L. Pintschovius, J. M. Bassat, P. Odier, F. Gervais, G. Chevrier, W. Reichardt, and F. Gompf, Phys. Rev. B **40**, 2229 (1989).

[43] M. F. Cetin, P. Lemmens, V. Gnezdilov, D. Wulferding, D. Menzel, T. Takayama, K. Ohashi, and H. Takagi, Phys. Rev. B **85**, 195148 (2012).

[44] P. Y. Yu and M. Cardona, *Fundamentals of Semiconductors: Physics and Materials Properties* (Springer, Berlin, 2005).

[45] D. Menzel, P. Popovich, N. N. Kovaleva, J. Schoenes, K. Doll, and A. V. Boris, Phys. Rev. B **79**, 165111 (2009).

[46] H. Zhang, K. Haule, and D. Vanderbilt, Phys. Rev. Lett. **111**, 246402 (2013).

[47] Q. Wang, Y. Cao, J. A. Waugh, S. R. Park, T. F. Qi, O. B. Korneta, G. Cao, and D. S. Dessau, Phys. Rev. B **87**, 245109 (2013).

[48] B. H. Kim, G. Khaliullin, and B. I. Min, Phys. Rev. Lett. **109**, 167205 (2012).

[49] K. Ishii, I. Jarrige, M. Yoshida, K. Ikeuchi, J. Mizuki, K. Ohashi, T. Takayama, J. Matsuno, and H. Takagi, Phys. Rev. B **83**, 115121 (2011).

[50] H. J. Park, C. H. Sohn, D. W. Jeong, G. Cao, K. W. Kim, S. J. Moon, H. Jin, D.-Y. Cho, and T. W. Noh, Phys. Rev. B **89**, 155115 (2014).